INTERFACE

royalsocietypublishing.org/journal/rsif

Research

Cite this article: Engels T, Wehmann H-N, Lehmann F-O. 2020 Three-dimensional wing structure attenuates aerodynamic efficiency in flapping fly wings. *J. R. Soc. Interface* **17**: 20190804.
http://dx.doi.org/10.1098/rsif.2019.0804

Received: 28 November 2019
Accepted: 14 February 2020

Subject Category:
Life Sciences–Physics interface

Subject Areas:
biomaterials, biomechanics, biomathematics

Keywords:
insect flight, aerodynamics, numerical modelling

Author for correspondence:
Fritz-Olaf Lehmann
e-mail: fritz.lehmann@uni-rostock.de

†These authors equally contributed to this work.

Electronic supplementary material is available online at https://doi.org/10.6084/m9.figshare.c.4865460.

THE ROYAL SOCIETY PUBLISHING

Three-dimensional wing structure attenuates aerodynamic efficiency in flapping fly wings

Thomas Engels[1,2,†], Henja-Niniane Wehmann[2,†] and Fritz-Olaf Lehmann[2]

[1]LMD-CNRS, École Normale Supérieure and PSL, 24 rue Lhomond, 75231 Paris Cedex 05, France
[2]Department of Animal Physiology, University of Rostock, Albert-Einstein-Strasse 3, 18059 Rostock, Germany

F-OL, 0000-0002-9511-3651

The aerial performance of flying insects ultimately depends on how flapping wings interact with the surrounding air. It has previously been suggested that the wing's three-dimensional camber and corrugation help to stiffen the wing against aerodynamic and inertial loading during flapping motion. Their contribution to aerodynamic force production, however, is under debate. Here, we investigated the potential benefit of three-dimensional wing shape in three different-sized species of flies using models of micro-computed tomography-scanned natural wings and models in which we removed either the wing's camber, corrugation, or both properties. Forces and aerodynamic power requirements during root flapping were derived from three-dimensional computational fluid dynamics modelling. Our data show that three-dimensional camber has no benefit for lift production and attenuates Rankine–Froude flight efficiency by up to approximately 12% compared to a flat wing. Moreover, we did not find evidence for lift-enhancing trapped vortices in corrugation valleys at Reynolds numbers between 137 and 1623. We found, however, that in all tested insect species, aerodynamic pressure distribution during flapping is closely aligned to the wing's venation pattern. Altogether, our study strongly supports the assumption that the wing's three-dimensional structure provides mechanical support against external forces rather than improving lift or saving energetic costs associated with active wing flapping.

1. Introduction

The aerial performance of flying insects depends on many factors and ultimately on how flapping wings interact with the surrounding air. Insect wings are complex composite structures that consist of stiff veins and elastic, interconnecting membranes with thicknesses of a few micrometres [1]. The wing venation pattern is species-specific and thus used for taxonomy [2–5]. Fine-scale geometrical wing structures are typically of much smaller scale than the primary flow structures at wings, such as wing-tip and leading-edge vortices, and referenced as wing corrugation [6]. Coarse-scale structures, by contrast, typically refer to the wing's overall curvature and are termed chordwise and spanwise wing camber [7].

Insect wings are largely passive structures and their three-dimensional shape and conformation vary as a result of external forces produced throughout the stroke cycle [8]. During flapping motion, wings dynamically deform due to changes in aerodynamic and inertial loading and thus deformation depends on two factors: the instantaneous local forces acting on both sides of the wing surface and the wing's local mechanical properties, governed by material strength and corrugation [8]. Corrugation amplitude typically tapers off towards the wing tip [9] and cross-veins help to maintain corrugation patterns under pressure load [1]. Chordwise corrugation is thought to enhance the wing's stiffness most effectively against bending but acts only little against torsion [10]. Thus, in many insects, this design allows reversible wing surface flattening

instead of irreversible plastic deformations under load [5]. Wing corrugation may also determine different bending and torsional behaviours during up- and downstroke [11], and thus controls changes in wing camber within the flapping cycle [12].

As corrugation pattern strongly determines the wing's stiffness distribution [1], it likely serves as a mechanical design element to avoid excessive wing deformation during flight rather than an element that helps to produce aerodynamic lift. In flies, for example, maximum corrugation occurs along spanwise veins that lie approximately one-third wing chord behind the leading edge of the wing [1]. At this wing section, the wing produces elevated aerodynamic pressure and thus needs elevated structural support [1]. Although corrugation is thought to have little effect on aerodynamic force production at small and intermediate Reynolds numbers [13], it may alter aerodynamic power requirements for flapping flight. Investigations on dragonfly and other insect model wings, for example, suggest that the latter effect results from flows trapped in the wing's zigzag corrugation valleys [9,14] or small, local changes in aerodynamic pressure [6].

In contrast with corrugation, the chordwise wing camber significantly changes the aerodynamic properties of a wing [12,15]. For example, the upward camber usually improves wing performance owing to an increase in the effective angle of attack, while the downward camber has the opposite effect [16]. In the first case, the wing's aerodynamic performance increases with decreasing distance between the leading wing edge and camber vertex [16]. Span- and chordwise camber dynamically changes during wing flapping, which alters the wing's aerodynamic performance throughout the stroke cycle [8,17–18] and helps to stabilize flight [19]. Owing to force-induced deformation, the camber is inverted (downward camber) in beetles during the upstroke, which improves aerodynamic performance compared to a non-deforming wing [12]. Aerodynamic details of wings with different geometry including twist, leading edge details and most relevantly camber have also been scored in hawkmoth-like revolving wings [20]. The authors found that flow separation at the leading edge prevents leading-edge suction and thus allows a simple geometric relationship between forces and angle of attack. The force coefficients in these experiments appear to be remarkably invariant against alterations in leading-edge detail, twist and camber. Nevertheless, our knowledge on the aerodynamic significance of three-dimensional wing structure in insect flight is rather limited and largely stems from studies that used simplified flight models such as two-dimensional computational simulations, rectangular flat wing planforms, simplified three-dimensional extrusions of two-dimensional profiles, and also from work at inappropriately large Reynolds number [9,13,15,21–26].

To overcome these limitations, we investigated the aerodynamic properties of three-dimensional wing shape in three different-sized species of flies using computational fluid dynamics (CFD). The wing models were reconstructed from high-resolution, micro-computed tomographic (µCT) scans. To dissect the contribution of fine- and coarse-scale structures to aerial performance, we numerically generated different sets of wings for each species and determined the benefit of individual wing structures for aerodynamic force production and flight power requirements. We scored the potential benefits at various Reynolds numbers and found that the three-dimensional wing structure has little impact on the mean vertical force production but alters the temporal distribution of forces during the stroke cycle via changes in the angle of attack. While the benefit for aerodynamic force production is little, wing corrugation and camber attenuate aerodynamic efficiency in three-dimensionally flapping insect wings that may increase the costs of flapping flight.

2. Material and methods

2.1. Morphological parameters and wing kinematics

We investigated wings from three different fly species: the fruit fly *Drosophila melanogaster* Canton S, the housefly *Musca domestica* and the blowfly *Calliphora vomitoria*. For better comparison, we used a generic stroke pattern [27] for all tested wings and adjusted fluid viscosity to match Reynolds number for wing flapping of each species (electronic supplementary material, table S1). Thus, any difference in aerodynamic properties between wing models of a single species can be attributed to differences in the wing's three-dimensional structure. The simulated wings flapped with 135° stroke amplitude and at angles of attack of 40° and 20° during up- and downstroke, respectively (figure 1*a*,*b*). The mean stroke plane was inclined by −20° with respect to the horizontal. At stroke reversals, the duration of wing rotation was 0.22 stroke cycle period, and both flapping motion and the changes in angles of attack at the reversals followed a sinusoidal time evolution. We scored aerodynamic properties at simulated forward flight with a velocity equal to 20% of the fly's wing tip velocity. A detailed description on how we derived these parameters is listed in the electronic supplementary material.

2.2. Reconstruction of model wings

We scanned twelve 2- to 6-day-old females of our laboratory strains (3 *Drosophila*, 3 *Musca*, 6 *Calliphora*) using a µCT scanner (Zeiss Xradia 410 Versa µCT, Carl Zeiss AG, Oberkochen, Germany). The final data were selected from a single animal of each species because even smallest movements of the animal during scanning prohibited an error-free reconstruction. The animals were placed into Dubosq-Brazil fixative for several days and subsequently incubated in Lugol's iodine for staining. For scanning, house- and blowflies were placed on a wet tissue into a closed tube to avoid desiccation, while fruit flies were scanned submerged in water. X-ray power varied between 2 and 8 W and optical magnification was 4× (*Drosophila*) and 0.4× (*Musca*, *Calliphora*). The edge length of the reconstructed cubic voxels was 3.5 µm in *Drosophila*, 7.4 µm in *Musca* and 10.6 µm in *Calliphora*. Image exposure times varied between 8 and 12 s and total scan time was 5–7.5 h for a single animal (figure 1*c*,*d*). We segmented the image, and also removed image noise and background using ICY software [28]. In cases in which the wing's alula or thin membranes near the trailing edge could not be reconstructed by µCT due to optical overlay, we combined X-ray scans with surface profile scans obtained from optical measurements with a profilometer (VR-3000, Keyence Corporation, Osaka, Japan) [29].

To estimate wing variability in the three species, we scored wing geometry in 16, 18 and 19 wings of *Drosophila*, *Musca* and *Calliphora*, respectively. We selected four characteristic points on the wing surface, measured the distance between these points and eventually normalized the measurements to wing size. In addition, we estimated the variance in wing contour and wing roughness. Methods and data are described in large detail in §1 of the electronic supplementary material. The

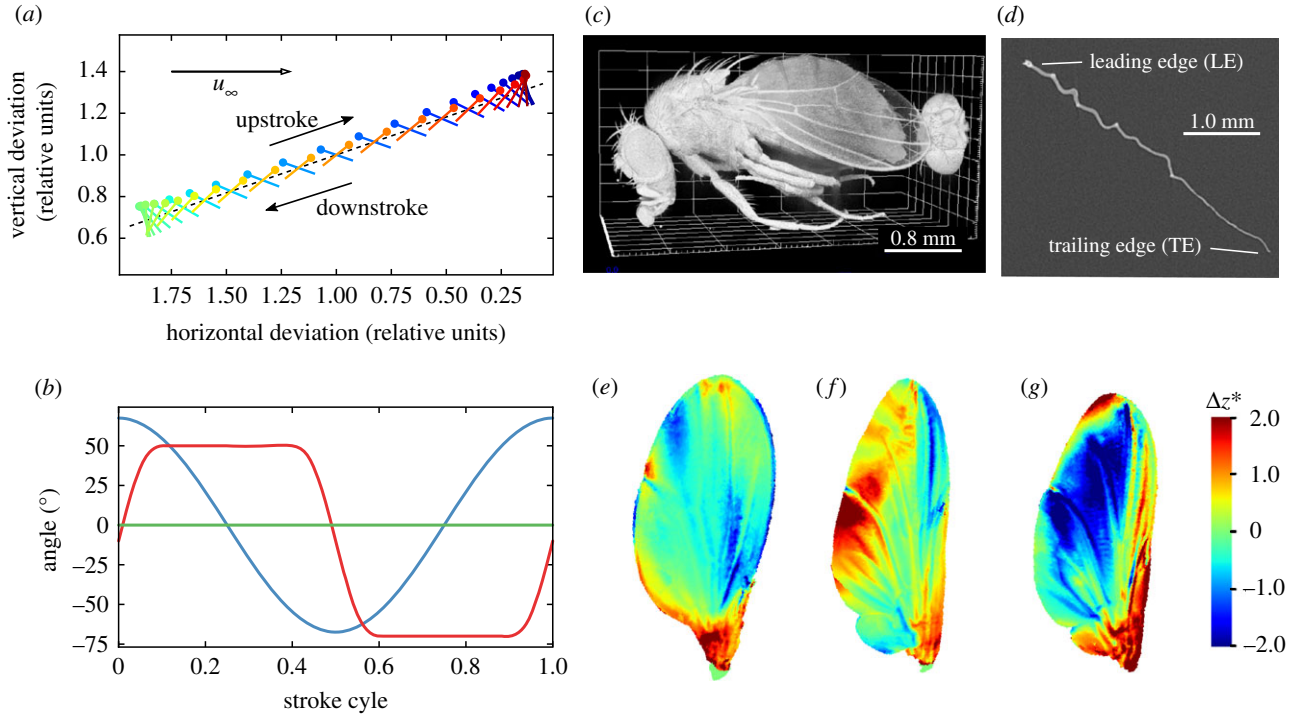

Figure 1. Wing kinematics and three-dimensional wing structure. (*a*) Angle of attack, up motion, down motion and heaving motion of a wing blade as used in the simulation. Dots mark the wing's leading edge and dashed line is the mean stroke plane. Oncoming flow u_∞ is from left to right. (*b*) Time evolution of positional angle (ϕ, blue), feathering angle (α, red) and deviation angle (θ, green) with respect to the stroke plane. (*c*) µCT-scanned image of a fruit fly *Drosophila*. Image shows a head of a second animal on the right. (*d*) Cross-section of the wing chord at 0.5 wing length of the blowfly *Calliphora*. (*e–g*) Local difference Δz^* between the tested wings in the simulation and mean wing surface structure of 16 wings in (*e*) (*Drosophila*), 18 wings in (*f*) (*Musca*) and 19 wings in (*g*) (*Calliphora*). Local difference was normalized by the standard deviation of each local surface pixel for better comparison. Data show that the wing used in the numerical simulation differs at most from the ensemble-averaged wings by twice the standard deviation of normalized wing height *z*. Data stem from wing measurements with an optical profilometer. See text for more details.

data show that there is only little variance in shape within a single species (electronic supplementary material, table S2 and figures S1 and S2). We found overall changes in wing geometry of approximately 2.9 ± 0.6% mean distance between the four selected points on the wing surface in *Drosophila*, approximately 2.8 ± 0.4% in *Musca* and approximately 3.0 ± 0.4% (means ± s.d.) in *Calliphora*. Variance in wing contour was negligible with maximum variance near the wing hinge at which wing velocity is small (electronic supplementary material, figure S2). Variance in surface roughness, i.e. the local difference between wing height *z* (cf. §2.3), of the simulated wing and ensemble-averaged wings was less than ±2 times the standard deviation of the surface means (figure 1*e–g*). The variance peaks at the wing's alula, the trailing edge and in structures near the wing base. In sum, in all tested species, we found that variance in three-dimensional wing geometry is relatively small. We thus neglected wing variance in this study.

Noteworthy, in this study, we did not model wing stiffness and elasticity, which is in line with numerous previous studies on the significance of corrugation in dragonfly [21–22,24–25,30–34], bumblebee [15,35], locust [36] and fruit fly wings [6]. These studies used rigid wings and ignored any elastic deformation during wing flapping while focusing on the aerodynamic effects of surface structure. In our study, this reduction in complexity of the parameter space is beneficial because forces and flows are attributable to the wing's corrugation and camber and not to changes in wing shape as a result of load-induced wing deformation. As our wing models are developed from fresh, hydrated wings attached to the animals, corrugation and camber approximate the wing's shape at its resting state. Thus, 'natural' camber and corrugation characterize the fly's wing structure free of inertial and aerodynamic loading. We discuss the limits of numerical simulations using rigid wing models in greater detail in §4 of the electronic supplementary material.

2.3. Separation of wing structures

To model three-dimensional wing geometry, we described the wings' top and bottom surfaces by the two functions $z_{top}(x_w, y_w)$ and $z_{bottom}(x_w, y_w)$, respectively, where x_w and y_w are coordinates in the wing frame of reference (figure 2*a*). The wing's local midplane z_w is the mean of both functions. Although wing length-normalized mean membrane thickness in flies is only approximately 0.01% [1,12,37–41], several previously published studies used an approximately 110-fold larger value (approx. 1.1%) for the mean membrane thickness [6,31–33,35,42]. Our CFD simulation required a minimum wing thickness of approximately 1.17% wing length that corresponds to a thickness of 28, 75 and 114 µm in *Drosophila*, *Musca* and *Calliphora*, respectively (electronic supplementary material, table S1). Wing thicknesses larger than the latter values were not affected by the minimum cut-off value.

As mentioned above, the minimum thickness is a requirement for our numerical simulation. Modern immersed boundary methods, like the volume penalization method in this study, approximate boundary conditions at the wing and body by supplementary terms in the Navier–Stokes equations. This is opposite to earlier methods that use body-conformal grids. The advantage of our method is that even highly complex, moving obstacles can be included with ease. Conventional grid generation, by contrast, requires significantly more computational work. However, if the wing becomes thinner than the grid resolution, the wing disappears in the simulation between two grid points. Thus, in practice, a minimum thickness of six grid points is required to satisfy boundary conditions.

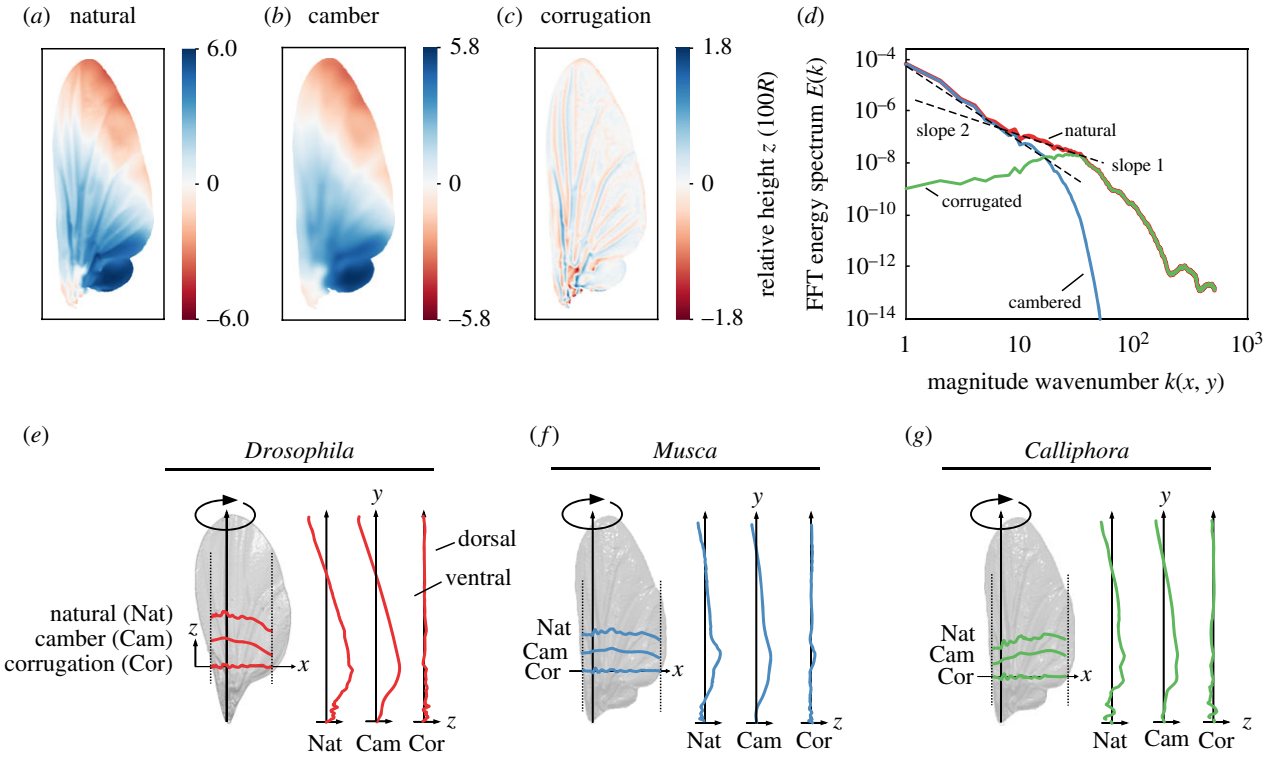

Figure 2. Decomposition of three-dimensional wing structure. (*a*) The surface of the µCT-scanned natural wing was filtered by high- and low-pass filters that generated model wings (*b*) with span- and chordwise camber but no corrugation and (*c*) with corrugation but no camber. (*d*) Filter coefficients were obtained from regression slopes fitted to the isotropic Fourier energy spectrum of the wing midplane. (*e–g*) Span- and chordwise wing profiles along the wings' axes of rotation. Data show profiles of all tested wings superimposed on natural wing models (grey). Note that the *z*-component is exaggerated by a factor of 2 for better clarity.

We used high- and low-pass filters to decompose z_w into coarse- (camber) and fine-scale (corrugation) structures, respectively (figure 2*b–g*). As the wing cut out from the µCT data produced a sharp transition between wing edges and ambient air, we first removed this transition. This was done by a numerical algorithm that generated a smooth extension of the wing's local plane z_w at the transition between the physical borders of the wing and the surrounding air. The extended z_w values were obtained via an iterative numerical process. The latter procedure solved a diffusion problem with Dirichlet boundary condition and is highlighted in detail in electronic supplementary material, figure S4. On the edge smoothed data, we eventually applied conventional filters for decomposition of wing structures. The filter coefficients were adjusted to separate the two distinct slopes present in the Fourier energy spectrum of the wing surface as a function of wavenumber magnitude (figure 2*d*; electronic supplementary material).

Secondly, we computed the Fourier transform as a function of the wavenumber $k = (k_x, k_y)$. To obtain wing corrugation, we applied the high-pass filter $g(k)$

$$g(k) = \exp\left[-((k_x - C_x)^2 + (k_y - C_y)^2)(2Q)^{-2}\right] \qquad (2.1)$$

to the Fourier coefficients. Wing camber was extracted using the corresponding low-pass filter $1 - g(k)$. In equation (2.1), integer wavenumbers are $0 \le k_{x,y} < N_{x,y}$, with $N_{x,y}$ the number of points of the extended data in each direction, $C_{x,y}$ the centre wavenumbers and Q the filter width parameter. To determine the filter parameters, we considered the wing's isotropic Fourier energy spectrum $E(k)$ (see electronic supplementary material). The two slopes in figure 2*d* show that the spectrum is divided into two fractions, corresponding to wing camber and corrugation. The filter parameters $C_{x,y} = 1/2N_{x,y}$ and $Q = 10$ separate both fractions. Using the above procedure, we generated four distinct, rigid wing models for each species. These were the originally measured wing (natural model; Nat), models with camber (Cam) but without corrugation, models with corrugation (Cor) but without camber, and completely flat models (Fla).

2.4. Numerical simulation

For CFD simulation, we used our previously published numerical code for flapping flight aerodynamics of insects (https://github.com/pseudospectators/FLUSI) [43–44]. The code is designed for high performance computing and uses a numerical grid that is fine enough to resolve all relevant fluid scales. Thus, there was no need for subgrid modelling. The simulations were performed with 16 384 CPU cores on an IBM BlueGene/Q machine located in Orsay, France. The three-dimensional computational domain was $2R \times 2R \times 2R$ with R the wing length and resolved by 1024 grid points in each dimension, yielding a total of 1.07 billion points. A vorticity sponge outflow condition was set at the domain borders [43]. The wing was modelled by the volume penalization method that approximates solid objects as a porous medium with small permeability [44,45]. Although volume penalization is well suited for large Reynolds numbers, high viscosity at low Reynolds numbers requires smaller permeability parameters and smaller simulation time steps. Moreover, as the wake typically first stabilizes some stroke cycles after wing motion onset, we scored the difference in aerodynamic performance between strokes in a series of computed cycles. In *Drosophila*, we found that the second cycle is already similar to the third one while in *Musca* and *Calliphora*, forces became stable in the fourth cycle owing to the larger Reynolds number. The shown data thus stem from the second (*Drosophila*) and fourth simulated stroke cycle (*Musca*, *Calliphora*). In all simulations, initial fluid velocity was equal to free stream velocity (electronic supplementary material, table S1) and wing flapping motion started impulsively. We simulated only the right wing and excluded the insect body. All forces were normalized

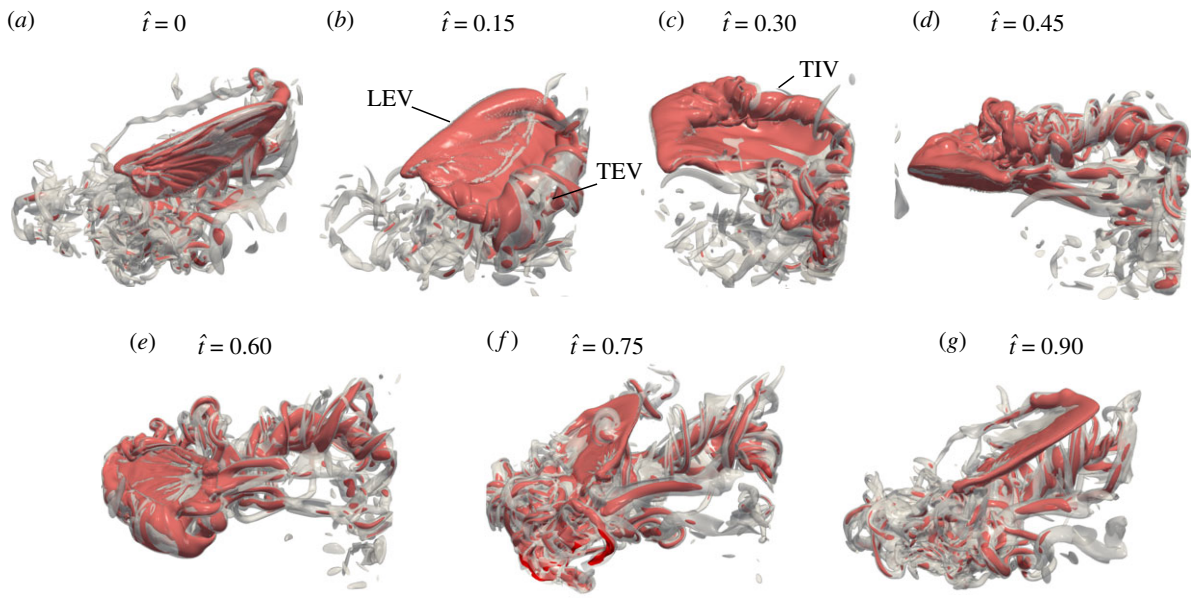

Figure 3. Flow structures during wing flapping. (*a–g*) Visualization of three-dimensional flow produced by a natural wing model of *Calliphora*. Data show iso-surface with vorticity magnitude of 50 s^{-1} (semi-transparent grey) superimposed on a vorticity iso-surface with 100 s^{-1} (red). The wing is shown at seven selected times of the stroke cycle (0–1), starting with the downstroke. LEV, leading-edge vortex; TEV, trailing-edge vortex; TIV, wing-tip vortex.

to the animal's body weight. From forces and velocities, we calculated flight muscle mass-specific aerodynamic power requirements and Rankine–Froude efficiency of wing flapping (see electronic supplementary material).

3. Results

3.1. General findings

All simulation runs of our CFD model produced flows and vortical structures similar to data previously published on flapping insect wings [46–50]. Figure 3*a–g* exemplarily shows typical flow structures at a natural model wing of *Calliphora*, such as the leading-edge vortex (LEV) and wing tip vortex (TIV). The vortices are visualized by iso-surfaces of vorticity magnitude at selected times of the stroke cycle.

3.2. Flow structures

It has previously been suggested that in a corrugated insect wing, surface valleys trap vortices and stagnant air. The trapped structures are thought to generate a beneficial aerodynamic profile that in turn increases the aerodynamic performance of the wing [9,14]. As characteristic length scales of the flow increase with decreasing Reynolds number, there was a higher chance of detecting trapped vortices in *Calliphora* than in *Drosophila*. Figure 4*a,b* shows instantaneous streamlines emitted from a line near the leading edge at natural and flat wings of both species. We found that the primary flow characteristics, i.e. leading edge and tip vortices, are similar in both wing models and both species. However, vortical flow at *Calliphora* wings appeared to be more turbulent, which was expected from the higher Reynolds number. Instantaneous force traces in *Drosophila* thus show less high-frequency force components compared to the larger species (see electronic supplementary material). This effect is most visible during the upstroke, at which the wing moves through the wake produced by the preceding downstroke.

In none of the fly wings did we find sufficient evidence for trapped vortices inside corrugation valleys (figures 4*c–e* and 5*a–c*). In figure 4*c–e*, we visualized the flow inside the valleys of natural wings between the wing's first and second, and between the second and third longitudinal veins using streamlines. The streamlines suggest that axial flow follows the pressure gradient from the wing base to wing tip at relatively low speed. We estimated velocities at approximately 0.3 wing length inside the valleys of less than approximately 0.15 m s^{-1} (*Drosophila*), approximately 1.6 m s^{-1} (*Musca*) and 2.2 m s^{-1} (*Calliphora*). These values are 6.4%, 31% and 32% of wing tip velocity in the three species, respectively (electronic supplementary material, table S1). The data also suggest that LEV suction pulls flow out of the valleys and away from the surface. Similar to velocity, vorticity inside the corrugation valleys is small and scattered around zero in all three tested species (figure 4*c–e*). In sum, we found that velocity is less than one-third of maximum velocity and vorticity is negligible in corrugation valleys of natural wings. This absence of trapped vortices is consistent with some previous studies on corrugated wings [31,51–53].

3.3. Force generation and power requirements

In all species, we found similar differences in force generation and power requirements among the four tested wing categories (natural, cambered, corrugated and flat wing design). At the selected stroke plane inclination of −20°, vertical force produced by a single natural wing compensates for approximately 0.23, approximately 0.70 and approximately 0.72 body weight in *Drosophila*, *Musca* and *Calliphora*, respectively (total force, table 1). An increase in vertical force production was at the cost of horizontal backward (negative) thrust of a single wing, i.e. approximately −0.10, approximately −0.20 and approximately −0.19 body weight, respectively (total force, table 1). In all tested wings, the kinematic pattern produced several-fold more positive vertical

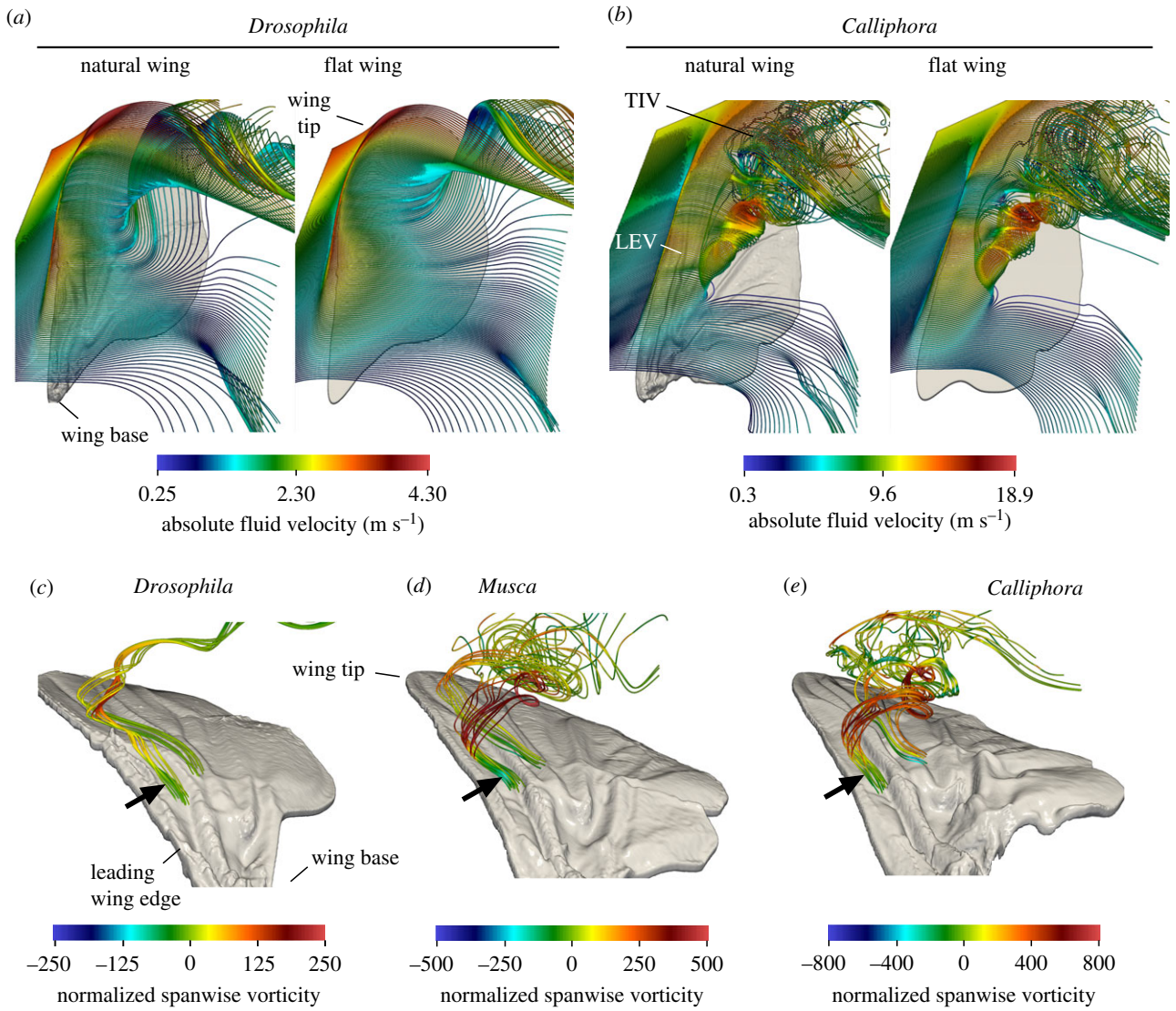

Figure 4. Flow pattern produced by natural and flat wing models. The flow is visualized at 1.3 and 3.3 stroke cycle at approximately mid-downstroke by instantaneous streamlines in (*a*) *Drosophila* and (*b*) *Calliphora*, respectively. Streamlines are computed from virtual particles released on a line below the wing and transported by the frozen instantaneous velocity field. Colour encodes fluid velocity. Velocity estimates are absolute values and were transformed into the rotating coordinate system of the wing. (*c–e*) Colour-coded instantaneous streamlines at 1.3 (*Drosophila*) and 3.3 stroke cycle (*Musca*, *Calliphora*) in natural wings. Streamlines were computed from particles released in the corrugation valleys of the dorsal (upper) wing surface near the leading wing edge. Data show little spanwise vorticity inside the corrugation valley near the surface (arrows) and leading-edge vortex suction pulls the virtual particles away from the surface.

force during the downstroke than during the upstroke (figure 6*a* and table 1). This temporal distribution is similar to the power stroke in flying birds [54]. The tested wings of all species produce rather similar instantaneous forces that peak at mid up- and downstroke owing to the wing's maximum translational velocity, and during the dorsal and ventral stroke reversals owing to wing rotation (figure 6*a*,*b*; see electronic supplementary material). This is similar to previously published CFD simulations and also to force measurements in robotic insect wings [50,55].

The natural wing model produces up to approximately 3% less mean vertical force than cambered, corrugated and flat wings of *Drosophila* and *Calliphora*. In *Musca*, by contrast, we find that the natural wing performs slightly better by up to approximately 6.7% vertical force, compared to wings with a reduced geometric structure (figure 6 and table 1). We found more pronounced changes in horizontal thrust production. In all flies, stroke-cycle averaged negative thrust (table 1), i.e. backward acceleration, decreases in modified wings compared to natural wings. In cambered wings, these changes are smallest, amounting to approximately 5.0%, approximately 8.1% and approximately 11% in *Drosophila*, *Musca* and *Calliphora*, respectively. Removing camber reduces the mean backward thrust by up to 39% in corrugated wings and up to 45% in flat wings, compared to natural wings (figure 6*d–f*). As camber changes the wing's geometrical angle of attack, the latter force changes might result from angular changes of the oncoming flow rather than from changes in the wing's aerodynamic characteristics. We tested this idea in §3.4.

The combination of both an increase in force production during the downstroke in modified compared to natural wings and backward orientation of the wing's mean force vector suggests that cycle-averaged drag is smaller in modified than in natural wings. In turn, this should lead to a decrease in total aerodynamic power requirements in modified wings. Figure 6*d–f* shows that flight muscle-mass specific aerodynamic power of flat wings indeed decreases

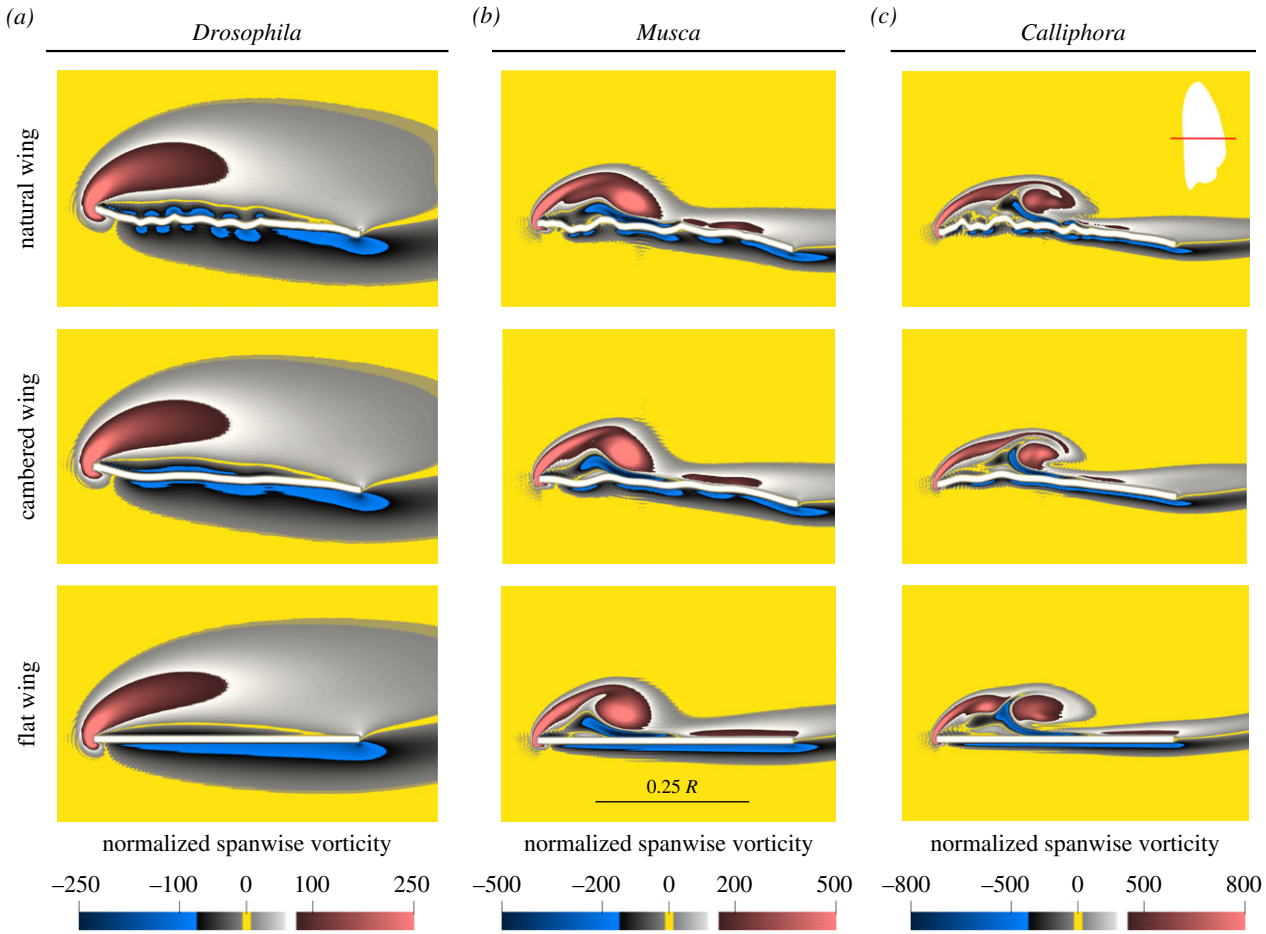

Figure 5. Vorticity distribution around a chordwise wing cross-section. (*a–c*) Spanwise vorticity around natural, cambered and flat wing models at 0.5 wing length and 1.3 simulated stroke cycle in (*a*) *Drosophila* (second stroke cycle) and 3.3 cycle in (*b*) *Musca* and (*c*) *Calliphora* (fourth stroke cycle, cf. §2.4). Thickness of wing profile in the simulation is explained in §2.3. *R*, wing length. Spanwise vorticity is normalized to wing stroke frequency of each fly species (electronic supplementary material, table S1) and thus dimensionless.

Table 1. Aerodynamic forces and power of tested wing models. $F^*_{vertical}$, body weight-specific vertical force acting against gravity (body lift); $F^*_{horizontal}$, body weight-specific horizontal force (body thrust); P^*_{aero}, flight muscle mass-specific aerodynamic power assuming that flight muscle mass equals one-third body mass. Wing structure is either natural as scanned by μCT, cambered by spatial low-pass filtering, corrugated by spatial high-pass filtering the natural wing, or completely flat. Data are time-averaged forces from the second (*Drosophila*) and fourth (*Musca*, *Calliphora*) stroke cycle. Up, half-cycle averaged force and power during wing upstroke; down, averaged force and power during wing downstroke; total, forces and power averaged over the entire wing stroke cycle.

		$\overline{F^*_{vertical}}$			$\overline{F^*_{horizontal}}$			$\overline{P^*_{aero}}$ (W kg^{-1})		
species	shape	up	down	total	up	down	total	up	down	total
Drosophila	natural	−0.03	0.48	0.23	0.06	−0.25	−0.10	8.08	28.0	18.1
	cambered	−0.02	0.48	0.23	0.06	−0.24	−0.09	8.10	27.5	17.8
	corrugated	−0.01	0.47	0.23	0.07	−0.20	−0.07	8.41	25.3	16.9
	flat	0.00	0.46	0.23	0.07	−0.20	−0.06	8.48	24.8	16.6
Musca	natural	0.04	1.37	0.70	0.11	−0.50	−0.20	37.1	158	97.5
	cambered	0.06	1.33	0.70	0.12	−0.48	−0.18	37.5	155	96.2
	corrugated	0.11	1.25	0.68	0.15	−0.39	−0.12	42.9	139	91.0
	flat	0.12	1.19	0.66	0.16	−0.37	−0.11	43.6	133	88.4
Calliphora	natural	0.04	1.40	0.72	0.11	−0.48	−0.19	39.7	204	122
	cambered	0.09	1.40	0.74	0.13	−0.46	−0.17	41.5	199	120
	corrugated	0.11	1.35	0.73	0.14	−0.43	−0.14	47.3	188	118
	flat	0.13	1.35	0.74	0.15	−0.42	−0.13	48.8	184	117

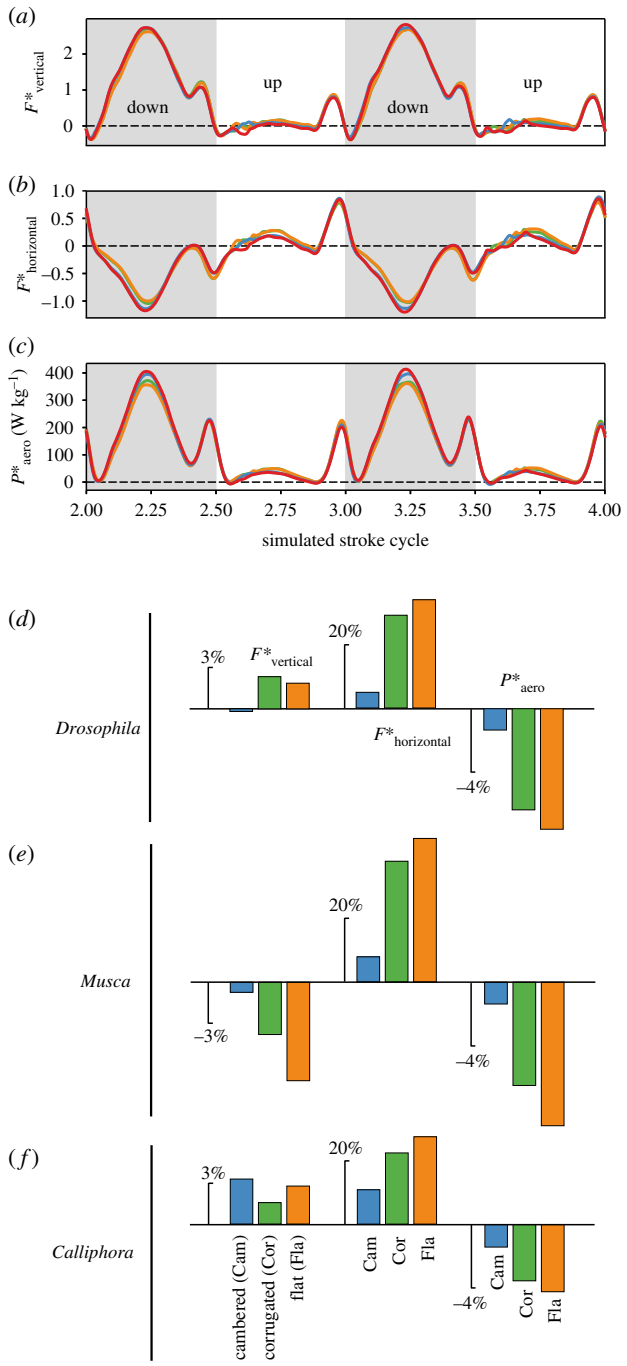

Figure 6. Time evolution and cycle-averaged change of vertical force, horizontal force and aerodynamic power. (*a–c*) Temporal alterations of body mass-specific vertical ($F^*_{vertical}$) and horizontal forces ($F^*_{horizontal}$), and flight muscle mass-specific aerodynamic power (P^*_{aero}) in *Calliphora*. Data were produced by the third and fourth wing stroke cycle after motion onset. Red, natural wing; blue, cambered wing; green, corrugated wing; orange, flat wing. (*d–f*) Relative change of cycle-averaged forces and power, compared to the performance of a natural wing of the blowfly.

up to approximately 7.9% (*Drosophila*), approximately 9.4% (*Musca*) and approximately 4.4% (*Calliphora*), compared to natural wings. There is no clear trend, though, thus it is less likely that these changes result from changing Reynolds number. On the contrary, it is surprising that there are only small differences in non-dimensional power requirements between species, considering that cycle-averaged muscle mass-specific power increases 6.7-fold from 18 W kg^{-1} in *Drosophila* to 120 W kg^{-1} muscle in *Calliphora*.

3.4. Wing camber, angle of attack and Rankine–Froude efficiency

In figure 7 we tested the simple idea that wing camber solely changes the wing's geometrical angle of attack during flapping, in turn altering force production during up- and downstroke rather than subtly changing the aerodynamic characteristics of a wing. For this control experiment, we solely used cambered and flat wing models of *Calliphora* because there was no need to investigate Reynolds number effects. We also simplified the kinematic pattern, removing the oncoming flow, stroke plane inclination angle and the difference in the angle of attack between up- and downstroke (see electronic supplementary material). We did this in order to remove flow and force asymmetries between the two half strokes when flapping a flat wing. Naturally cambered wings should alter this stroke symmetry because camber in our rigid wing is thought to decrease the angle of attack during the upstroke and increase it during the downstroke. A symmetrical up- and downstroke emphasizes this effect and makes the results more easily accessible.

Figure 7*a,b* shows the time evolution of vertical force and aerodynamic power of a cambered wing, respectively, as a function of the geometrical angle of attack during wing translation. At zero angle of attack, the wing is horizontally aligned during the translation phase but generates positive (negative) vertical forces during the downstroke (upstroke) owing to its upward camber in chordwise direction. At the stroke reversal, a cambered wing with zero angle of attack produces maximum vertical forces because of the large 180° rotational angle. Figure 8*a* shows how half-cycle and cycle-averaged vertical forces change with increasing angle of attack in a cambered wing. The horizontally shifted curves suggest that in wing models with camber, vertical force increases (decreases) during the downstroke but likewise decreases (increases) during the upstroke for angles of attack less than 50° (greater than 50°). A comparison with forces computed for a flat, non-cambered wing (orange, figure 8*a*) shows that there is no benefit in cycle-averaged vertical force from wing camber for wing kinematics with a symmetrical up- and downstroke.

While a flat wing produces equal amounts of vertical force during up- and downstroke at the selected kinematics, wing camber unbalances the temporal distribution of forces within the stroke cycle. This changes moments (yaw, pitch, roll) and also aerodynamic power requirements. We tested the latter prediction and calculated flight muscle mass-specific aerodynamic power for wings at various angles of attack (figure 8*b*). The data show a local minimum in cycle-averaged power requirements at approximately 20° angle of attack that is despite even slightly higher vertical force production at this angle (figure 8*a*), approximately 8% smaller in a flat compared to a cambered wing. Consequently, the Rankine–Froude efficiency is up to approximately 9% higher for a flat than a cambered wing (figure 8*c*). Efficiency peaks in both wings at approximately 30–40° angle of attack. Thus, in the tested case, wing camber increases flight costs without providing a benefit for body weight support. This result also holds for data derived for *Drosophila* (approx. 12% lower Froude efficiency) and *Musca* (approx. 5% lower efficiency; for wing kinematics, see figure 1). As expected from aerodynamic theory, we also found that Froude efficiency in a flat wing increases with increasing Reynolds

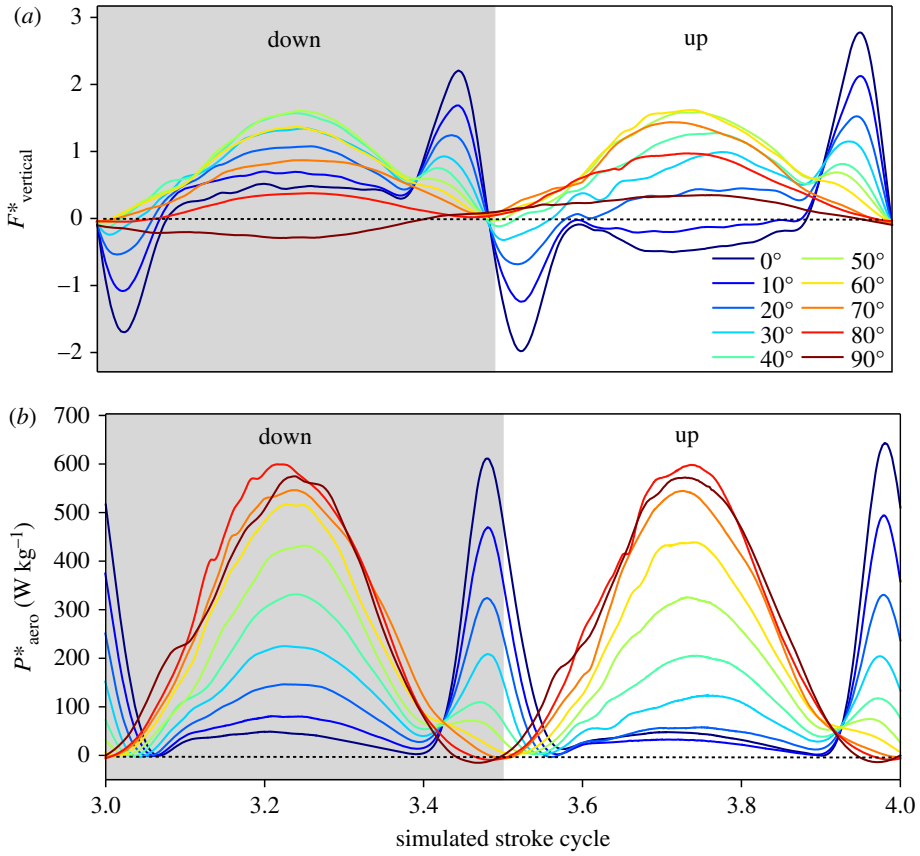

Figure 7. Forces and power at wing motion with different angle of attack. (*a*) Time evolution of vertical force and (*b*) aerodynamic power generated by a cambered wing of *Calliphora* flapping in the horizontal and with identical angles of attack during up- and downstroke (see electronic supplementary material). Colours indicate the wing's angle of attack.

number, amounting to 0.17, 0.21 and 0.23 in *Drosophila*, *Musca* and *Calliphora*, respectively (natural, 0.15, 0.22, 0.21; cambered, 0.15, 0.22, 0,23; corrugated wing, 0.17, 0.22, 0.23; respectively).

3.5. Surface pressure and wing venation

Previous studies have shown that fly wing venation and corrugation determine the wing's mechanical properties including wing camber and elastic deformation [1,9–11,22,29]. From this perspective, wing veins predominately shape insect wings and control shape under aerodynamic and inertial loading. Here, we show that wing vein support reflects the distinct low-pressure regions of fly wings caused by LEV suction force. From our CFD simulations, we calculated the difference of pressure acting on the ventral and dorsal wing side throughout the stroke cycle of a natural *Calliphora* wing model (for wing kinematics, see figure 1*a*), with positive values indicating suction pressure normal to the dorsal wing surface. For better comparison, we normalized the pressure difference by a reference pressure. This reference value is equal to the wings' uniform and homogeneous load distribution $m_b g A_w^{-1}$, with m_b the body weight, g the gravitational constant and A_w the surface of two wings.

Figure 9 shows the wing's aerodynamic suction pattern during the downstroke. The pattern follows the development of leading-edge vorticity after the dorsal stroke reversal. Suction and thus vertical force approximately peak at mid-downstroke (0.25 stroke cycle) and subsequently decrease when the wing decreases its flapping velocity (0.3–0.4 stroke cycle, figure 9). The pressure distribution shows that the zones of elevated pressure difference are remarkably well concentrated to those wing membranes (wing cells) that are enclosed by strong veins. Elevated suction pressure up to 12 Δp^* (figure 9) is limited to areas between the leading wing edge and the fifth longitudinal vein and thus to the anterior wing cells and first and second posterior cells. In wing areas at the trailing edge such as the third posterior cell, suction pressure is negligible. This cell is not surrounded by wing veins, allowing elevated elastic deformation in the flying fly. Moreover, pressure and venation patterns together suggest that the local bending moments might bend an elastic wing more at the distal part than at its proximal part because of the hinge-to-tip gradient in vein density. We also found that the specific pressure pattern in figure 9 persists in all tested wing models of all three species (figure 10) and is thus independent of camber and corrugation. In sum, the latter findings suggest that elevated stiffness at the wing's leading edge provides structural support not only for inertial loading during wing acceleration but also for elevated aerodynamic loading owing to the LEV.

4. Discussion and conclusion

4.1. General remarks

For decades, the significance of three-dimensional wing structure in insects for aerodynamic force production and power consumption has puzzled biologists and engineers. Our simulations suggest that the coarse structure of fly wings (camber) has a pronounced effect on the temporal

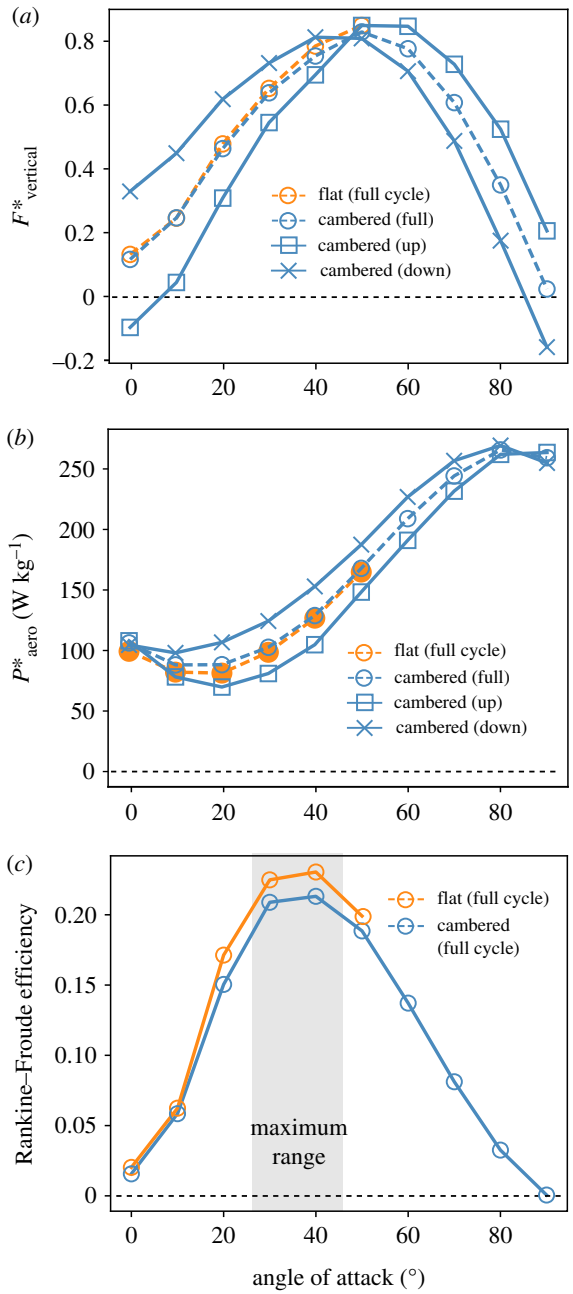

Figure 8. Vertical force, power and Rankine–Froude efficiency in flat (orange) and cambered (blue) wings. (*a*,*b*) Polar plots of vertical force and aerodynamic power plotted as a function of angle of attack. Data show the performance of wings of *Calliphora* averaged over a full stroke cycle (full cycle), over the upstroke (up) and over the downstroke (down). (*c*) Data show cycle-averaged performance of the fourth simulated wing stroke cycle produced by wings of *Calliphora*. Efficiency was calculated from data shown in (*a*,*b*).

distribution of aerodynamic forces within the stroke cycle. This effect is likely due to a change in the wing's geometrical angle of attack (figures 7 and 8). We found no pronounced benefit in cycle-averaged vertical force production in cambered wings compared to flat, non-cambered wings. Additionally, in all tested fly species, the Rankine–Froude efficiency of vertical force production is smaller (or equal) in natural than in flat wings. Within the tested range of Reynolds numbers, by contrast, fine wing structures change aerodynamic forces only little and we found no evidence for vortex trapping in corrugation valleys. The latter result runs counter to previous findings on insect wings at higher Reynolds number and will be discussed in the following section, while other aspects of wing corrugation are discussed afterwards.

4.2. Vortex trapping

It has previously been suggested that air, trapped in corrugation valleys of insect wings, improves lift production owing to a profiled wing cross-section [9,14]. Vortices and even stagnant air cushions may thus alter a wing's effective geometry. Trapped vortices were experimentally found in wings moving at relatively high Reynolds number [52–53], including an aerodynamic study that showed vortex trapping at Reynolds numbers between 34 000 and 100 000 but not at 3500 [33]. The latter value is at the upper end of Reynolds numbers typical for flying insects. Other authors who studied flows of a flapping beetle model wing [12] attributed an absence of vortex trapping to the elevated angle of attack in insect wings. Nevertheless, as the authors removed camber from the corrugated beetle wing model, the wing exhibited aerodynamic characteristics similar to profiled NACA0005 model wing. An absence of trapped flows has also been shown in corrugated wings of gliding dragonflies [24,31]. Altogether, little corrugation, low Reynolds number, spanwise flow advecting vorticity and high angle of attack apparently hinder vortex trapping in flapping insect wings. It is thus not surprising that we did not find clear evidence for trapped vortices in our fly wings at Reynolds numbers up to 1623. Consequently, we suggest that trapped, lift-enhancing flows in dragonfly wings should be considered as an exception rather than a common aerodynamic phenomenon in insect flight. This finding is also consistent with a comprehensive review on corrugated aerofoils. In this review, the authors present evidence that corrugated aerofoils are not thought to improve aerodynamic performance as hypothesized by other researchers [56].

4.3. Significance of three-dimensional wing design

There is an ongoing controversy on the benefit of wing corrugation for aerodynamic performance in insect wings. Some authors find an improvement in performance owing to corrugation [9,15,21,23,25,51], while other authors argue that corrugation attenuates performance [13,22,26]. It is likely that in part these conflicting results arise from the use of different CFD models and different Reynolds numbers. Numerical studies that report changes typically used two-dimensional simulations at high Reynolds number ($Re > 5000$). By contrast, studies that find little or no effect typically tend to use three-dimensional numerical models at Reynolds numbers between 35 and 3500. The latter is in the range of an average-sized insect. Although corrugation may change local wing pressure, the difference of lift and drag coefficients between corrugated and flat wings is typically not more than 5% for lift and 17% for drag ($Re = 200$, angle of attack 5°) [6,35]. It is likely that the size ratio (wing–vortex interaction) between corrugation structure and LEV, or corrugation structure and the area of flow separation, is key for the changes described above [6]. As the size of flow structures depends on Reynolds number, corrugation structures should be more coarse in small insects than in larger animals for pronounced wing–vortex interaction. As the corrugation pattern on the dorsal wing side is inverted on the ventral wing side, wing–vortex interference should be even

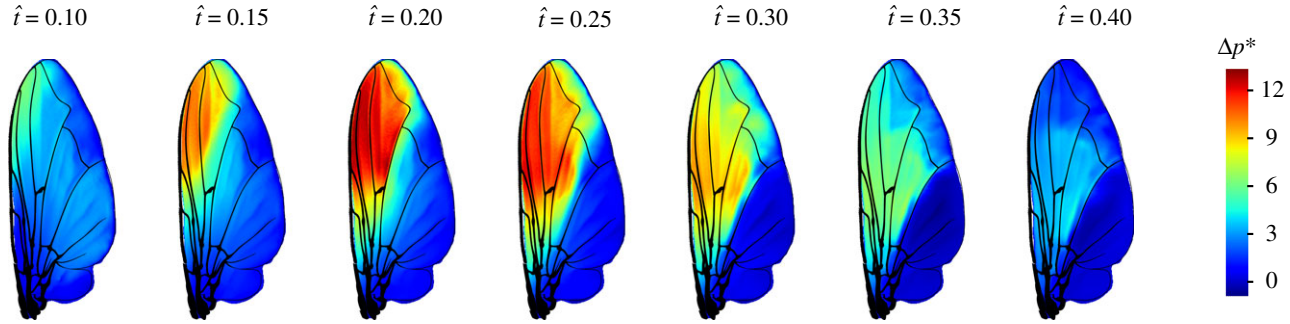

Figure 9. Time evolution of pressure distribution within a flapping cycle. Pressure is shown as the difference (Δp^*) between the aerodynamic pressures acting on ventral and dorsal wing sides. The pressure difference is normalized to the mean wing loading, i.e. half the body mass. Forces resulting from pressure are orientated normal to local wing surface. Positive values indicate suction pressure on the dorsal wing surface. Data show pressure distribution during the fourth simulated stroke cycle and were computed using the natural wing model of *Calliphora*.

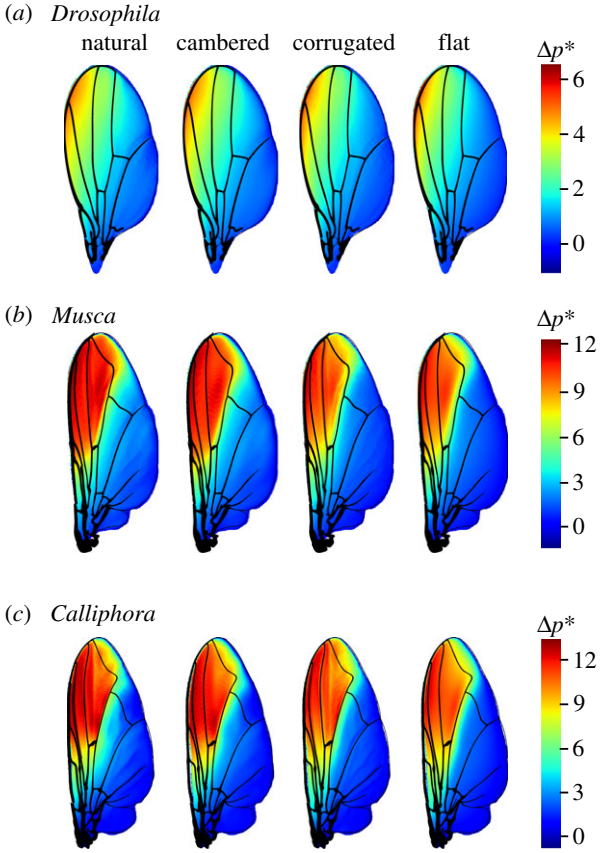

Figure 10. (*a–c*) Pressure difference between ventral and dorsal wing sides of all tested wing models and fly species. Pressure difference (Δp^*) is normalized to the mean wing loading (see legend to figure 9 and text) and forces derived from pressure are orientated normal to local wing surface. Pressure was scored at 0.2 stroke cycle at the beginning of the downstroke. Note that wing venation is shown on all wings even though its geometrical contribution to the three-dimensional wing structure has been removed in cambered and flat wing models.

different during up- and downstroke, as should aerodynamic performance and power requirements.

4.4. Conclusion

Our data show that the three-dimensional design of fly wings determines aerodynamic force production, power requirements and Rankine–Froude efficiency. Although the differences in vertical force production and aerodynamic power requirements between cambered, corrugated and flat wings are relatively minor, we found elevated changes in horizontal thrust and flight efficiency. The computed flight efficiencies of 17–23% are somewhat below experimentally derived estimates that range from 26–32% in various species of fruit flies to 37–55% in large crane flies, beetles and bees [57]. The limits and difficulties of power estimation in flapping flight of insects, though, were recently highlighted by a numerical study using lifting line formulations [58]. Notably, our findings are restricted to the selected kinematic pattern and also ignore elastic wing deformation during flapping motion. For example, elastic corrugated hoverfly model wings are more effective than elastic flat wings (+3% vertical force, −3% aerodynamic power, $Re = 800$) [59], while corrugated but rigid hoverfly wings lose their ability to produce maximum vertical force compared to a flat rigid wing [59]. We found that the impact of Reynolds number on aerodynamic performance is inconsistent, which is most likely due to the relatively small range of tested numbers. We suggest that a comprehensive understanding of the functional benefit of camber, corrugation and elasticity requires more elaborate numerical and physical wing models than those previously presented. These test beds should also include fluid–structure interaction and consider a vast variety of kinematic patterns as they occur during manoeuvring flight. In sum, the overlap between wing venation pattern and elevated local aerodynamic pressure strongly supports the hypothesis that wing corrugation adds structural support to a wing, rather than improving aerodynamic performance. Even if there are some energetic costs associated with corrugation, corrugation might be of elevated advantage during conditions that have not been tested in this study—such as extreme wing loading during manoeuvring flight and flight under turbulent environmental conditions.

Data accessibility. All data needed to evaluate the conclusions in the paper are present in the paper itself and in the electronic supplementary material or are available from the Dryad Digital Repository: http://doi.org/10.5061/dryad.z612jm68c.

Authors' contributions. T.E. designed the study, carried out data fusion and numerical simulations and drafted the manuscript; H.-N.W. acquired the experimental data, segmented the µCT scans, participated in the design of the study and drafted the manuscript; F.-O.L. conceived of the study, participated in the design of the study and critically revised and edited the manuscript. All authors gave final approval for publication and agree to be held accountable for the work performed therein.

Competing interests. We declare we have no competing interests.

Funding. This work was financially supported by grant no. 15-CE40-0019 of the French Agence Nationale de la Recherche (ANR), grant nos. SE824/26-1 and LE905/17-1 of the German Science Foundation (DFG) and the French–German PROCOPE project FIFIT

funded by the Ministères des Affaires Etrangères et du Développement International (MAEDI) et de l'Education Nationale, de l'Enseignement Supérieur et de la Recherche et de l'Innovation (MENESRI) and Deutscher Akademischer Auslandsdienst (DAAD). Simulations were due to access to the HPC resources of IDRIS and TGCC under the allocation 2018-1664 made by GENCI and to the HPC resources of Aix-Marseille University financed by the project Equip@Meso (grant no. ANR-10-EQPX-29-01).

Acknowledgements. The authors thank S.N. Gorb and L. Heepe at the University of Kiel for use of the profilometer, C. Wirkner and S. Scholz for help with the µCT, and the unknown referees for their helpful comments on the manuscript.

References

1. Rees CJC. 1975 Form and function in corrugated insect wings. *Nature* **256**, 200–203. (doi:10.1038/256200a0)
2. Comstock JH. 1918 *The wings of insects: an exposition of the uniform terminology of the wing-veins of insects and a discussion of the more general characteristics of the wings of the several orders of insects*. Ithaca, NY: Comstock Publishing Company.
3. Rognes K. 1991 *Blowflies (Diptera, Calliphoridae) of Fennoscandia and Denmark*. Leiden, The Netherlands: E. J. Brill/Scandinavian Science Press Ltd.
4. Tofilski A. 2004 DrawWing, a program for numerical description of insect wings. *J. Insect Sci.* **4**, 17. (doi:10.1093/jis/4.1.17)
5. Newman DJS, Wooton RJ. 1986 An approach to the mechanics of pleating in dragonfly wings. *J. Exp. Biol.* **125**, 361–372.
6. Luo G, Sun M. 2005 The effects of corrugation and wing planform on the aerodynamic force production of sweeping model insect wings. *Acta Mech. Sin.* **21**, 531–541. (doi:10.1007/s10409-005-0072-4)
7. Koehler C, Liang Z, Gaston Z, Wan H, Dong H. 2012 3D reconstruction and analysis of wing deformation in free-flying dragonflies. *J. Exp. Biol.* **215**, 3018–3027. (doi:10.1242/jeb.069005)
8. Wootton RJ. 1999 Invertebrate paraxial locomotory appendages: design, deformation and control. *J. Exp. Biol.* **202**, 3333–3345.
9. Kesel AB. 2000 Aerodynamic characteristics of dragonfly wing sections compared with technical aerofoils. *J. Exp. Biol.* **203**, 3125–3135.
10. Sunada S, Zeng L, Kawachi K. 1998 The relationship between dragonfly wing structure and torsional deformation. *J. Theor. Biol.* **193**, 39–45. (doi:10.1006/jtbi.1998.0678)
11. Wootton RJ. 1993 Leading edge section and asymmetric twisting in the wings of flying butterflies (insecta, papilionoidea). *J. Exp. Biol.* **180**, 105–117.
12. Le TQ, Truong TV, Tran HT, Park SH, Ko JH, Park HC, Yoon KJ, Byun D. 2013 Two- and three-dimensional simulations of beetle hind wing flapping during free forward flight. *J. Bionic. Eng.* **10**, 316–328. (doi:10.1016/S1672-6529(13)60227-9)
13. Meng XG, Mao S. 2013 Aerodynamic effects of wing corrugation at gliding flight at low Reynolds numbers. *Phys. Fluids* **25**, 071905. (doi:10.1063/1.4813804)
14. Rees CJC. 1975 Aerodynamic properties of an insect wing section and a smooth aerofoil compared. *Nature* **258**, 141–142. (doi:10.1038/258141a0)
15. Feaster J, Battaglia F, Bayandor J. 2017 A computational study on the influence of insect wing geometry on bee flight mechanics. *Biol. Open* **6**, 1784–1795. (doi:10.1242/bio.024612)
16. Okamoto M, Yasuda K, Azuma A. 1996 Aerodynamic characteristics of the wings and body of a dragonfly. *J. Exp. Biol.* **199**, 281–294.
17. Young J, Walker SM, Bomphrey RJ, Taylor GK, Thomas ALR. 2009 Details of insect wing design and deformation enhance aerodynamic function and flight efficiency. *Science* **325**, 1549–1552. (doi:10.1126/science.1175928)
18. Zheng L, Hedrick TL, Mittal R. 2013 Time-varying wing-twist improves aerodynamic efficiency of forward flight in butterflies. *PLoS ONE* **8**, e53060. (doi:10.1371/journal.pone.0053060)
19. Mistick EA, Mountcastle AM, Combes SA. 2016 Wing flexibility improves bumblebee flight stability. *J. Exp. Biol.* **219**, 3384–3390. (doi:10.1242/jeb.133157)
20. Usherwood JR, Ellington CP. 2002 The aerodynamic of revolving wings I. Model hawkmoth wings. *J. Exp. Biol.* **205**, 1547–1564.
21. Chen Y, Skote M. 2016 Gliding performance of 3-D corrugated dragonfly wing with spanwise variation. *J. Fluid Struct.* **62**, 1–13. (doi:10.1016/j.jfluidstructs.2015.12.012)
22. Hord K, Liang Y. 2012 Numerical investigation of the aerodynamic and structural characteristics of a corrugated airfoil. *J. Aircraft* **49**, 749–757. (doi:10.2514/1.C031135)
23. Jain S, Bhatt VD, Mittal S. 2015 Shape optimization of corrugated airfoils. *Comp. Mech.* **56**, 917–930. (doi:10.1007/s00466-015-1210-x)
24. Kim W-K, Ko JH, Park HC, Byun D. 2009 Effects of corrugation of the dragonfly wing on gliding performance. *J. Theor. Biol.* **260**, 523–530. (doi:10.1016/j.jtbi.2009.07.015)
25. Levy D-E, Seifert A. 2009 Simplified dragonfly airfoil aerodynamics at Reynolds numbers below 8000. *Phys. Fluids* **21**, 071901. (doi:10.1063/1.3166867)
26. Tanaka H, Okada H, Shimasue Y, Liu H. 2015 Flexible flapping wings with self-organized microwrinkles. *Bioinsp. Biomim.* **10**, 046005. (doi:10.1088/1748-3190/10/4/046005)
27. Lehmann F-O, Gorb S, Nasir N, Schützner P. 2011 Elastic deformation and energy loss of flapping fly wings. *J. Exp. Biol.* **214**, 2949–2961. (doi:10.1242/jeb.045351)
28. de Chaumont F *et al.* 2012 Icy: an open bioimage informatics platform for extended reproducible research. *Nat. Meth.* **9**, 690–696. (doi:10.1038/nmeth.2075)
29. Wehmann H-N, Heepe L, Gorb SN, Engels T, Lehmann F-O. 2019 Local deformation and stiffness distribution in fly wings. *Biol. Open* **8**, bio038299. (doi:10.1242/bio.038299)
30. Vargas A, Mittal R, Dong H. 2008 A computational study of the aerodynamic performance of a dragonfly wing section in gliding flight. *Bioinspir. Biomim.* **3**, 026004. (doi:10.1088/1748-3182/3/2/026004)
31. Barnes CJ, Visbal MR. 2013 Numerical exploration of the origin of aerodynamic enhancements in low-Reynolds number corrugated airfoils. *Phys. Fluids* **25**, 115106. (doi:10.1063/1.4832655)
32. Flint TJ, Jermy MC, New TH, Ho WH. 2017 Computational study of a pitching bio-inspired corrugated airfoil. *Int. J. Heat Fluid Flow* **65**, 328–341. (doi:10.1016/j.ijheatfluidflow.2016.12.009)
33. Shahzad A, Hamdani HR, Aizaz A. 2017 Investigation of corrugated wing in unsteady motion. *J. Appl. Fluid Dyn.* **10**, 833–845. (doi:10.18869/acadpub.jafm.73.240.26425)
34. Ansari MI, Anwer SF. 2018 Numerical analysis of an insect wing in gliding flight: effect of corrugation on suction side. *Fluid Dyn. Mater. Process.* **14**, 259–279. (doi:10.32604/fdmp.2018.03891)
35. Meng X, Sun M. 2011 Aerodynamic effects of corrugation in flapping insect wings in forward flight. *J. Bionic. Eng.* **8**, 140–150. (doi:10.1016/S1672-6529(11)60015-2)
36. Xiang J, Du J, Li D, Liu K. 2016 Aerodynamic performance of the locust wing in gliding mode at low Reynolds number. *J. Bionic. Eng.* **13**, 249–260. (doi:10.1016/S1672-6529(16)60298-6)
37. Appel E, Heepe L, Lin C-P, Gorb SN. 2015 Ultrastructure of dragonfly wing veins: composite structure of fibrous material supplemented by resilin. *J. Anat.* **227**, 561–582. (doi:10.1111/joa.12362)
38. Ren H, Wang X, Li X, Chen Y. 2013 Effects of dragonfly wing structure on the dynamic performances. *J. Bionic. Eng.* **10**, 28–38. (doi:10.1016/S1672-6529(13)60196-1)
39. Tanaka H, Wood RJ. 2010 Fabrication of corrugated artificial insect wings using laser micromachined molds. *J. Micromech. Microeng.* **20**, 075008. (doi:10.1088/0960-1317/20/7/075008)
40. Xiang J, Du J, Li D, Zhen C. 2016 Functional morphology and structural characteristics of wings of the ladybird beetle, *Coccinella septempunctata*

(L.). *Microsc. Res. Tech.* **79**, 550–556. (doi:10.1002/jemt.22669)

41. Zhao Y, Tong J, Sun J. 2014 Microstructure of the wings of dragonfly *Pantala flavenscens* Fabricius and finite element analysis of its mechanical property. *Optoelectron. Adv. Mat.* **8**, 794–799.
42. Aono H, Liu H. 2013 Flapping wing aerodynamics of a numerical biological flyer model in hovering flight. *Comp. Fluids* **85**, 85–92. (doi:10.1016/j.compfluid.2012.10.019)
43. Engels T, Kolomenskiy D, Schneider K, Sesterhenn J. 2015 Numerical simulation of fluid-structure interaction with the volume penalization method. *J. Comp. Phys.* **281**, 96–115. (doi:10.1016/j.jcp.2014.10.005)
44. Engels T, Kolomenskiy D, Schneider K, Sesterhenn J. 2016 FluSI: a novel parallel simulation tool for flapping insect flight using a Fourier method with volume penalization. *SIAM J. Sci. Comp.* **38**, S3–S24. (doi:10.1137/15M1026006)
45. Angot P, Bruneau CH, Fabrie P. 1999 A penalization method to take into account obstacles in incompressible viscous flows. *Numer. Math.* **81**, 497–520. (doi:10.1007/s002110050401)
46. Suzuki N, Miyata H, Ishiwata S, Kinosita Jr K. 1996 Preparation of bead-tailed actin filaments: estimation of the torque production by the sliding force in an in vitro motility assay. *Biophys. J.* **70**, 401–408. (doi:10.1016/S0006-3495(96)79583-8)
47. Engels T, Kolomenskiy D, Schneider K, Lehmann F-O, Sesterhenn J. 2016 Bumblebee flight in heavy turbulence. *Phys. Rev. Lett.* **116**, 028103. (doi:10.1103/PhysRevLett.116.028103)
48. Aono H, Liu H. 2006 Vortical structure and aerodynamics of hawkmoth hovering. *J. Biomech. Sci. Eng.* **1**, 234–245. (doi:10.1299/jbse.1.234)
49. Lehmann F-O. 2000 Vorticity in insect flight. In *3rd International Workshop on Similarity Methods* (eds B Kröplin, S Rudolph, S Brückner), pp. 85–91. Stuttgart, Germany: University of Stuttgart.
50. Dickinson MH, Lehmann F-O, Sane S. 1999 Wing rotation and the aerodynamic basis of insect flight. *Science* **284**, 1954–1960. (doi:10.1126/science.284.5422.1954)
51. Kim Y, Peskin CS. 2009 3-D parachute simulation by the immersed boundary method. *Comp. Fluids* **38**, 1080–1090. (doi:10.1016/j.compfluid.2008.11.002)
52. Murphy JT, Hu H. 2010 An experimental study of a bio-inspired corrugated airfoil for micro air vehicle applications. *Exp. Fluids* **49**, 531–546. (doi:10.1007/s00348-010-0826-z)
53. New TH, Chan YX, Koh GC, Hoang MC, Shi S. 2014 Effects of corrugated aerofoil surface features on flow-separation control. *AIAA J.* **52**, 206–211. (doi:10.2514/1.J052398)
54. Dhawan S. 1991 Bird flight. *Sadhana* **16**, 275–352. (doi:10.1007/BF02745345)
55. Liu H, Ellington CP, Kawachi K, Berg CVD, Willmott AP. 1998 A computational fluid dynamic study of hawkmoth hovering. *J. Exp. Biol.* **201**, 461–477.
56. Lian Y, Broering T, Hord K, Prater R. 2014 The characterization of tandem and corrugated wings. *Progr. Aero. Sci.* **65**, 41–69. (doi:10.1016/j.paerosci.2013.08.001)
57. Lehmann F-O. 2001 The efficiency of aerodynamic force production in *Drosophila*. *Comp. Biochem. Physiol. Part A* **131**, 77–88. (doi:10.1016/S1095-6433(01)00467-6)
58. Nabawy MRA, Crowthe WJ. 2015 A quasi-steady lifting line theory for insect-like hovering flight. *PLoS ONE* **10**, e0134972. (doi:10.1371/journal.pone.0134972)
59. Du G, Sun M. 2012 Aerodynamic effects of corrugation and deformation in flapping wings of hovering hoverflies. *J. Theor. Biol.* **300**, 19–28. (doi:10.1016/j.jtbi.2012.01.010)